Case Studies in Thermal Engineering 71 (2025) 106228

Contents lists available at ScienceDirect

Case Studies in Thermal Engineering

journal homepage: www.elsevier.com/locate/csite

Waste-to-energy: Pyrolysis-gasification conversion of packaging waste from both micro and macro perspectives

Zhitong Yao [a], Denzel Christopher Makepa [b], Sourav Poddar [c,d], Markus Reinmöller [e], Michael Bertelsen [e,*], Jingjing Jiang [a], Jiayao Tong [a], Jiuzhuo Cui [a], Jie Liu [a], Ivan Miguel De Cachinho Cordeiro [f,**]

[a] College of Materials Science and Environmental Engineering, Hangzhou Dianzi University, Hangzhou, 310018, China
[b] Department of Fuels and Energy Engineering, Chinhoyi University of Technology, Private Bag 7724, Chinhoyi, Zimbabwe
[c] Department of Chemical Engineering, National Institute of Technology, Tiruchirappalli, 620015, India
[d] Department of Chemical Engineering, Haldia Institute of Technology, West Bengal, 721657, India
[e] Technical University of Denmark, DTU Engineering Technology, Ballerup, 2750, Denmark
[f] School of Mechanical and Manufacturing Engineering, University of New South Wales, Sydney, NSW, 2052, Australia

GRAPHICAL ABSTRACT

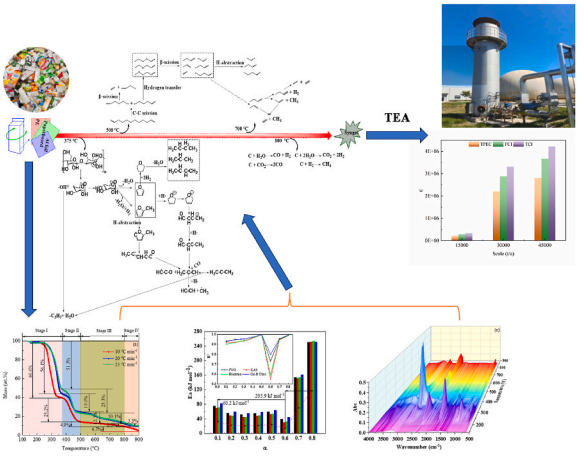

* Corresponding author.
** Corresponding author.
E-mail addresses: miber@dtu.dk (M. Bertelsen), i.decachinhocordeiro@unsw.edu.au (I.M. De Cachinho Cordeiro).

https://doi.org/10.1016/j.csite.2025.106228
Received 14 January 2025; Received in revised form 26 March 2025; Accepted 29 April 2025
Available online 3 May 2025

ARTICLE INFO

Keywords:
Packaging waste
Post consumer-beverage cartons
Pyrolysis-gasification conversion
ReaxFF-MD simulation
Techno-economic analysis

ABSTRACT

The increasing volume of packaging waste, a representative component of municipal solid waste, has raised considerable environmental concerns. The present study conducted a detailed investigation into kinetic and thermodynamic of pyrolysis-gasification for post-consumer beverage cartons (BCs). Subsequently, the conversion was simulated using reactive force field molecular dynamics (ReaxFF-MD) to outline a proposed conversion pathway. Techno-economic assessment (TEA) was then conducted to evaluate economic performance of BCs conversion at different scales. The BCs decomposition could be divided into four stages of <375, 375–500, 500–800 and 800–900 °C with mass loss of 51.3–60.6, 19.0–25.3, 4.9–12.3 and 2.5–4.7 wt%, respectively. Fourier transform infrared spectrometry and mass spectrometry confirmed the evolution of olefins, alkynes, and diolefins. The mean activation energy was calculated to be 60.2 kJ mol^{-1} within conversion of <0.60, which increased significantly to 205.9 kJ mol^{-1} for greater conversions. Positive changes in enthalpy and Gibbs free energy confirmed the endothermic and non-spontaneous nature of the pyrolysis-gasification reaction. The products generated and reactions involved in ReaxFF-MD simulation corresponded with the mass spectrometry results, indicating that β-scission of radicals was the predominant pathway for olefin formation. TEA analysis revealed that larger plants (45000 tonnes/a) had greater revenue potential, profitability, and positive returns on investment.

Nomenclature

List of abbreviations

BCs	Beverage cartons
ReaxFF-MD	Reactive force field molecular dynamics
TEA	Techno-economic assessment
FTIR-MS	Fourier transform infrared spectrometry and mass spectrometry
MSW	Municipal solid waste
PE	Polyethylene
HDPE	High-density polyethylene
TCI	Total capital investment
FCI	Fixed capital investment
WC	Working capital
TDIC	Total direct and indirect costs
PC	Project contingency
TIC	Total installed costs
IC	Indirect costs
TPEC	Total purchased equipment

List of variables and indices

β	Heating rate, K min^{-1}
α	Degree of conversion
A	Pre-exponential factor, min^{-1}
T	Temperature, K
f(α)	Kinetic model function
g(α)	Integral form of f(α)
$\frac{d\alpha}{dt}$	Conversion rate
p(x)	Temperature integral
R	Universal gas constant, 8.314 J/(mol·K)
R^2	Coefficient of correlation
ΔH	change in enthalpy, kJ mol^{-1}
ΔS	Change in entropy, kJ mol^{-1} K^{-1}
ΔG	Change in Gibbs free energy, kJ mol^{-1}
K_b	Boltzmann constant, 1.38E-23 J K^{-1}
h	Planck constant, 6.63E-34 Js
T_p	Peak temperature from derivative thermogravimetry, K

1. Introduction

Conventional fossil fuels currently account for about 82 % of global energy consumption. In the 21st century, the imperative to reduce our heavy reliance on non-renewable resources and mitigate significant pollution they generate has become increasingly urgent. The necessity for clean energy is further heightened by the confluence of rapid population growth, industrialization, and demand for sustainable global development. It is therefore imperative to implement long-term strategies that promote renewable energy sources and enhance energy efficiency reducing carbon emissions and achieving carbon neutrality [1]. Gasification is an environmentally friendly conversion that can transform organic compounds into syngas at high temperatures and controlled oxygen levels [2,3]. It offers several environmental advantages, providing an alternative to landfilling and addressing energy security concerns, particularly in conflict-affected regions. Significant progresses have been achieved in reactor design, catalyst development, as well as engineering scale-up through extensive research. However, numerous technical challenges remain, including the design and scale-up of reactors, optimization of entire system through process integration, and techno-economic evaluation. These factors ultimately influence the commercial viability of gasification process.

Gasification has been predominantly conducted using coal as the primary feedstock. However, the conversion of diverse organic waste presents significant challenges due to their heterogeneous compositions. Packaging waste, constituting 15–20 wt% of total municipal solid waste (MSW) in various countries, represents a significant challenge in solid waste management [4]. In 2021, the EU produced approximately 84 million tonnes packaging waste making up over a third of all MSW [4]. A similar trend is observed in the USA and Australia, with packaging waste accounting for 30–35 wt% of the annual MSW generation. Beverage cartons (BCs) are commonly composed of paperboard, polyethylene (PE), and aluminum foil and are utilized for milk, juice, and yogurt packaging. In China, waste BCs represent about 15 wt% of MSW, whereas in numerous European countries, this proportion exceeds 30 wt%. In 2019, 51 wt% of BCs entering the EU market were successfully recycled, whereas in China, the recycling rate was as low as ~20 wt%. The remaining waste is frequently commingled with other refuse or incinerated in an improper manner. It is therefore imperative that effective recycling strategies for packaging waste are developed in order to address environmental concerns and foster sustainable growth in packaging industry. Given the substantial quantities of paper and plastic present in packaging materials, thermal conversion represents a viable option for the recovery of energy and fuel [5,6]. Siddiqui et al. [7] pyrolyzed aluminium-plastic laminates over zeolites, resulting in the production of aromatic compounds. Wang et al. [8] employed hydrothermal treatment to recover bio-oil from similar waste materials. Haydary et al. [9] conducted pyrolysis of beverage cartons, yielding non-condensable gases comprising predominantly of H_2, CO, CH_4, and light hydrocarbons. Given the heterogeneous nature of this feedstock, it is critical to gain a full understanding of the degradation process and mechanisms in order to scale up and design effective reactors. Nevertheless, a notable deficiency in comprehensive research on this subject impedes the practical implementation of large-scale applications. In addition, a major challenge is to capture detailed structure changes at the micro level, including radicals and intermediates involved in matrix dissociation and vapor phase reactions. Consequently, the fundamental mechanisms of gasification and the pathways of fuel gas formation remain poorly understood.

Reactive force field molecular dynamics (ReaxFF-MD) simulation [10,11], represents an effective methodology for the investigation of intricate reaction systems, wherein the specific reaction pathways remain undetermined. It has been widely employed to study intricate macromolecular systems, including polymers, coal, and biomass. This approach focuses on reaction mechanisms, product distribution, intermediates, and role of free radicals. For example, Xuan et al. [12] applied ReaxFF-MD simulation to investigate the gasification conversion of PE. Similarly, Hong et al. [13] investigated coal pyrolysis, while Pang et al. [14] examined the reaction mechanism of lignin gasification using this methodology. Furthermore, Cordeiro et al. [15] employed ReaxFF-MD simulation to examine thermal decomposition of high-density polyethylene (HDPE). Although numerous studies have demonstrated its efficiency in elucidating mechanisms of chemical reactions involved in macromolecular oxidation and pyrolysis, researches on the decomposition of BCs remain scarce. Accordingly, the kinetic and thermodynamic parameters of BCs pyrolysis-gasification were studied in this study. Furthermore, ReaxFF-MD was utilized to ascertain the intermediates involved at the atomic level and to propose a fundamental reaction mechanism. Finally, TEA was performed to evaluate the feasibility of BCs gasification.

2. Materials and methods

2.1. Raw materials

BCs sampled from a local MSW transfer station was subjected to a cleansing process utilizing deionized water. Following cleaning, the material was dried in oven and cut into small pieces. Then, these pieces were ground using a high-speed rotary grinder (FM200, Beijing Geruideman Instrument Equipment Co. Ltd., China) under nitrogen and sieved using a no. 200 mesh (<74 μm) to achieve the desired consistency.

2.2. Experimental procedure

Thermogravimetric analysis is widely used for the kinetic analysis of various fuels. In this study, a thermogravimetric analyzer (STA 449 F3, Netzsch, Germany) was used. Samples with weight of ~10 mg were placed in crucibles and heated to desired temperatures under argon atmosphere maintained at a flow rate of 20 ml min^{-1}. The temperature was initially raised to ~140 °C to ensure complete removal of moisture. The samples were then heated to 900 °C in the presence of both steam and argon. The evolved products were analyzed through a thermal analyzer coupled with Fourier-transform infrared spectroscopy, while their composition was further

investigated using a quadrupole mass spectrometer (Clarus SQ 8T, PerkinElmer, USA).

2.3. Kinetic modeling

Kinetic modeling theories are outlined here with further discussions available in literatures [16–19]. Two principal methods are commonly used to analyze the decomposition of solids: model-fitting and -free approaches. Model-free techniques do not rely on predefined assumptions about the data distribution, offering greater flexibility and the capacity to accommodate different types of data. However, this flexibility may result in a reduction in accuracy. In contrast, model-fitting methods use predefined models to analyze the data. If an appropriate model is chosen, these methods can achieve high accuracy, but their reliability depends on the validity of model chosen. The selection of two methods depends on characteristics of data set, analytical objectives and assumptions about the underlying reaction mechanisms.

The Arrhenius equation is fundamental to understanding the influence of temperature on reaction rates and is the basis of extensive scientific research in this field. It is expressed as:

$$\frac{d\alpha}{dT} = \frac{\mathrm{A}}{\beta} e^{-\frac{E_a}{RT}} \times f(\alpha) \tag{1}$$

where α refers to the degree of conversion. The β and f(α) stand for heating rate (K min^{-1}) and reaction mechanism, respectively. The pre-exponential factor, represented by the symbol A, is given in min^{-1}, while the activation energy (Ea) is expressed in kJ mol^{-1}.

By rearranging eq. (1), the following equation can be obtained.

$$g(\alpha) = \int_0^{\alpha} \frac{d\alpha}{f(\alpha)} = \frac{\mathrm{A}}{\beta} \int_{T_0}^{T} e^{-\frac{E_a}{RT}} dT = \frac{AE_a}{\beta R} p(x) \tag{2}$$

Where g(α) represents the temperature integral approximation and its value is influenced by specific reaction mechanism being considered. In this study, four models including Friedman, Flynn-Wall-Ozawa (FWO), Kissinger-Akahira-Sunose (KAS), and Cai & Chen were used to determine the Ea values. The results obtained from these models were then compared to identify the most reliable model.

For Coats-Redfern (CR) model, a linear fit is performed by plotting $ln\frac{g(\alpha)}{T^2}$ against $\frac{1}{T}$ based on a given β and proposed g(α). The regression yields a slope of $-\frac{E_a}{R}$ and intercept of $\ln\frac{AR}{\beta E_a}$, which were used to calculate the values of E_a and A, respectively. The master-plots method has proven to be an effective approach for elucidating solid-state reaction mechanism. It involves comparing the experimental curve with theoretical ones. Further details can be found in previous report [17], where the common reaction models were outlined.

2.4. Thermodynamic analysis

The concept of enthalpy provides an insight into the heat changes associated with a reaction. The change in enthalpy (ΔH) indicates whether a reaction is exothermic or endothermic. Entropy quantifies the degree of disorder in a thermodynamic system. A negative values of change in entropy (ΔS) indicate a decrease in disorder, whereas a positive value indicates an increase in disorder. Gibbs free energy is the amount of energy available to drive a chemical reaction. The ΔH, ΔG, and ΔS values are calculated using eqs. (5)–(7) [20, 21].

$$\Delta H = E_a - R \cdot T \tag{5}$$

$$\Delta G = E_a + R \cdot T_p \, ln\frac{k_b T_p}{hA} \tag{6}$$

$$\Delta S = \frac{\Delta \mathrm{H} - \Delta \mathrm{G}}{\mathrm{T}_p} \tag{7}$$

where k_b represents the Boltzmann constant. The symbol h denotes the Planck constant and T_p refers to maximum peak temperature.

2.5. ReaxFF-MD simulation method

Fig. S1 shows a schematic diagram of ReaxFF-MD simulation for reference. The molecular structure of BCs comprises cellulose and PE. Cellulose chains were assembled by polymerizing 1,4-β-D-glucopyranose monomers via glycosidic bonds, resulting in a polymerization degree of 27. Conversely, PE was synthesized from ethylene monomers with a polymerization degree of 35. The cellulose and PE chains were incorporated into a periodic domain with dimensions of 200 Å × 200 Å × 200 Å, comprising a total of 866 atoms with a cellulose-to-PE mass ratio of 7:3. To simulate the steam gasification of BCs sample, the periodic box was filled with 1096 water molecules using the PACKMOL software. The water molecules were distributed to ensure a safe pairwise distance between them, with a feedstock ratio of 3. The domain was then subjected to energy minimization using the FIRE algorithm and equilibrated for 50 ps at 298 K. During this process, domain deformation was applied to compress the model until a reaction density of 0.96 g/cm^3 was achieved. The final dimensions of the periodic domain were 35 Å × 35 Å × 35 Å. The interatomic interactions among C, H, and O atoms were

governed by ReaxFF CHO force field as introduced by Chenoweth et al. [22].

To investigate the effects of reaction temperature and time on products evolution, all simulations were performed using NVT ensemble method. A Nose-Hoover chain (NHC) thermostat was used to control the temperature. Isothermal simulations were performed at 1800, 2500, and 3000 K for 500 ps to observe oxidation reactions, ensuring sufficient atomic motion and molecular collisions within the constraints of available computational resources.

2.6. Methodology of TEA

The BCs are sourced from MSW within a 250 km radius of the proposed gasification plant. Three processing scales 15,000, 30,000, and 45,000 tonnes/a are considered, representing small, medium, and large-scale gasification plants, respectively, based on typical waste generation rates. Waste collection was performed using covered trucks with a maximum payload capacity of 20 tonnes. Transport costs were calculated based on one-way distance, payload, and average diesel prices. At the gasification plant, the waste was shredded and pre-treated to remove unprocessable materials such as metals. The pre-treated waste was then fed into a downdraft gasifier operating at atmospheric pressure. Steam was used as gasifying agent, achieving a thermal efficiency of 60 %. The resulting syngas was fed to an onsite power generation unit using a gas engine or micro gas turbine for combined heat and power production.

TEA is an important tool for evaluating assessing the feasibility of gasification power plant [23–26]. In this study, a TEA was carried out for three syngas-to-power plants with different capacities to assess financial viability. The estimation of capital costs started with the selection of appropriate equipment based on mass and energy balances. The prices of the required equipments were obtained from industrial suppliers to determine total cost of purchased equipment (TPEC). Fig. S2 outlines the calculation of total capital investment (TCI), including TPEC, installation costs, instrumentation and piping (I&P), electrical components, and contingency costs. Key performance indicators (KPIs) such as specific capital cost (SCC), return on investment (ROI) and payback period (PBP) were analyzed to assess the profitability of plants.

2.6.1. TCI estimation

This study used the factorial method to estimate TCI. It derives capital costs from purchased equipment costs by applying multiplying factors and provides greater accuracy than rapid or step-count methods [27]. The process began with the determination of TPEC for major equipment items. The remaining components of TCI were then calculated as multiples of TPEC, following the investment factors outlined by Peters and Timmerhaus, as detailed in Fig. S2 [28]. For all equipment except compressors and turbines, TCI was assumed to be 200 % of TPEC. A project contingency (PC) of 20 % was added to account for total direct and indirect costs (TDIC) was incorporated. In addition, working capital (WC) was estimated at 15 % of fixed capital investment (FCI). Finally, the TCI was calculated based on FCI and WC.

2.6.2. Economic assumptions and criteria

TEA modeled the plant as a fully owned capital asset, assuming 80 % operating availability (7000 h/a) and a project lifetime of 20 years. These assumptions were consistent with evaluations of small to medium plants. Estimated cost of purchasing feedstock was set at €100/tonne, while waste collection and transport costs were set at €2.0/tonne and €7.5/tonne, respectively. Pretreatment costs were fixed at €0.02/tonne and a waste disposal subsidy of €15/tonne was applied. In addition, the project benefit from corporate income tax exemptions for the first three profitable years, followed by a reduced rate of 50 % for years four to six.

The key economic metrics were derived from TCI estimate. The SCC, which represents the capital requirements per kWh of annual production, was calculated using the following formula:

$$SCC = \frac{TCI}{Annual\ electricity\ production\ (\mathrm{kWh})} \tag{8}$$

Gross profit (GP), including depreciation was calculated annually for each year (n = 1 to 20) using the following equation.

$$GP_n = ASR_n - TPC_n - DC_n \tag{9}$$

where ASR_n is the annual sales revenue. TPC_n refers to the total production cost, and DC_n represents the depreciation cost.

ASR was determined as:

$$ASR = EPR\ (kWh/a) \times electricity\ price\ (€/\mathrm{kWh}) \tag{10}$$

The total production cost consists of fixed operating expenses and feedstock/utility costs. PBP measures the time required for cumulative cash flows (CF) to equal FCI. This metric is essential for evaluating capital recovery timelines and is calculated as follow.

$$PBP = \frac{FCI}{GP_{avg} + DC_{avg}} = \frac{0.87 \times TCI}{CF_{avg}} \tag{11}$$

where FCI approximates 87 % of TCI based on the methodology for calculating TCI components. ROI expresses average annual GP as a percentage of TCI.

$$ROI(\%) = 100 \times \frac{GP_{avg}}{TCI} \tag{12}$$

Discounted cash flow rate of return (DCFROR), also known as the internal rate of return, is defined as the interest rate (i) which satisfies the following condition.

$$NPV_N = \sum_{n=1}^{N} \frac{CF_n}{(1+i)^n} = 0 \tag{13}$$

3. Results and discussion

3.1. TG-FTIR-MS analysis

Fig. 1 shows the TG-FTIR-MS analysis for the decomposition of BCs. TG curves (Fig. 1a) indicated a total mass loss of 90.0–95.5 wt %, which was higher than that reported under other atmospheres. For example, Siddiqui et al. [29] observed mass losses of 80.0 and 82.6 wt% for two BCs samples below 800 °C in nitrogen. Similarly, Figen et al. [30] reported weight reductions of 88–90.1 wt% for carton boards, and Huo and Ma [31] found a mass loss of 89.4 wt% in CO_2. The higher mass loss in present study was primarily due to the reduced char formation and enhanced char gasification reactions within the steam atmosphere. Xu et al. [32] showed that increasing steam concentration markedly reduced char yields and facilitated char condensation. Mellin et al. [33] also observed that the introduction of steam during biomass pyrolysis resulted in a decrease in char yield compared to other atmospheres. Fig. 1b illustrates the DTG curves for both paperboard and PE components fitted using a Gaussian distribution model with a multi-peak method in originlab software. The close match between DTG curve and Gaussian fit confirmed the accuracy of this model.

The decomposition of BCs could be divided into four stages, based on temperature and corresponding weight loss. The initial stage, occurring below 375 °C, demonstrated a notable decomposition of BCs, resulting in a mass loss of 51.3–60.6 wt%. The sharpest peak temperatures were recorded at 278, 340, and 342 °C, which correspond to three different heating rates. Cellulose fibers constitute the primary component of BCs and their volatilization typically occurs between 250 and 400 °C. Therefore, the mass loss observed in this stage resulted from the decomposition of paperboard. This finding was consistent with previous studies, for instance, Alvarenga et al. [34] attributed the mass loss at 300–420 °C to paperboard devolatilization, confirmed by a comparison of peak temperatures for carton, individual paperboard, and PE. Similarly, Siddiqui et al. [29] reported weight reductions of 35.4 and 23.8 wt% for two BCs samples with different paper contents at 100–380 °C.

In stage II (375–500 °C), a weight loss of 19.0–25.3 wt% was observed, with peak temperatures recorded at 425, 438, and 440 °C for the three heating rates. The presence of a single peak in DTG curve implied that plastic degradation predominantly followed a single-step mechanism. Siddiqui et al. [29] revealed mass losses as 35.4 and 23.8 wt% for two BCs samples and attributed to the discrepancy to variations in PE content. Alvarenga et al. [34] indicated that PE devolatilization occurred at 400–550 °C. Saad et al. [35] observed peaks of 480 and 474 °C for the degradation of LDPE under N_2 and CO_2 atmospheres, respectively.

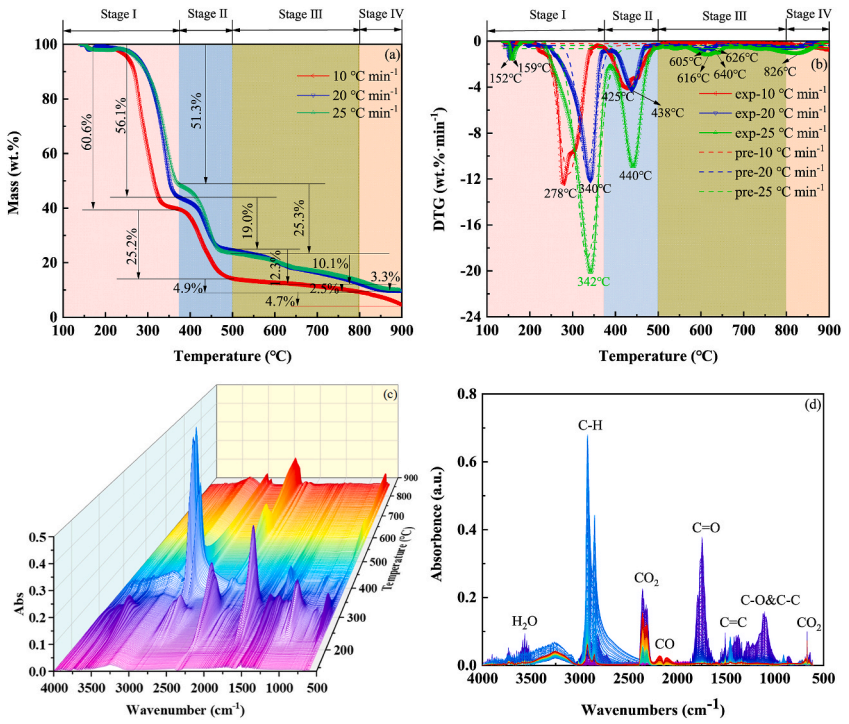

Fig. 1. TG (a, b)-FTIR (c-e)-MS (f–i) analysis of BCs decomposition.

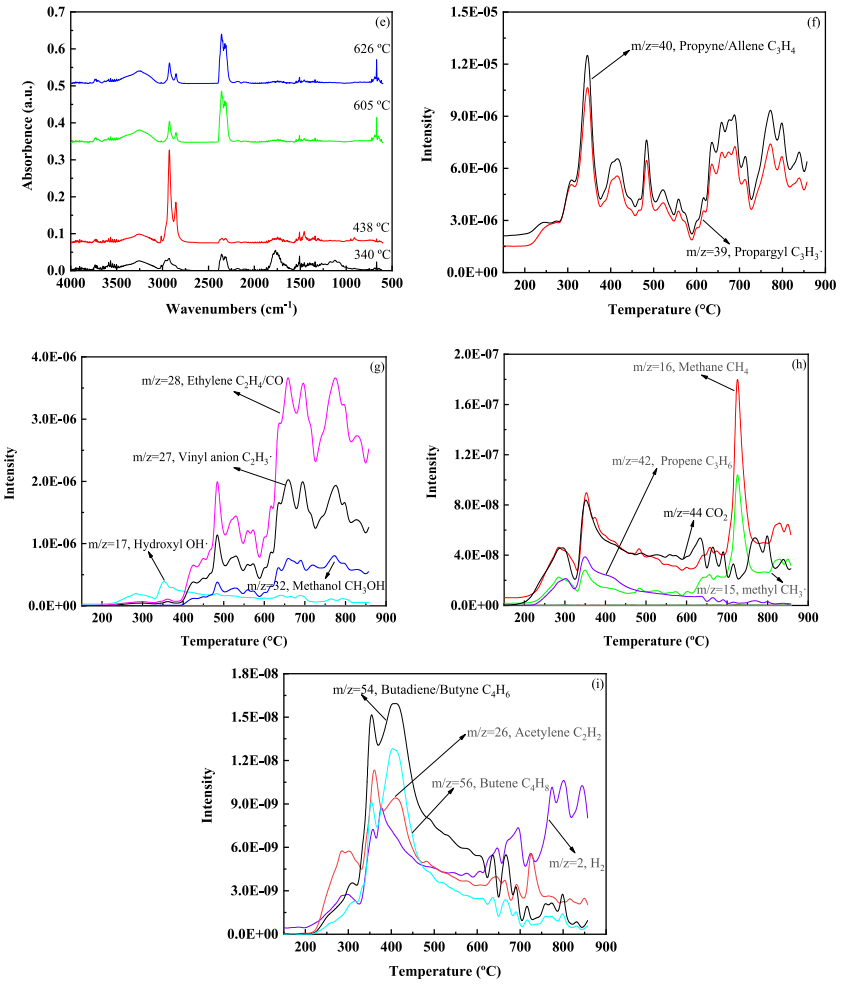

Fig. 1. (*continued*).

In stage III (500–800 °C), a relatively low weight of 4.9–12.3 wt% was observed. Following the degradation of cellulose and devolatilization of PE, the release of volatiles from the sample matrix played a crucial role in char formation. Trapped volatiles can be charred, while repolymerization or condensation of intermediates further contributes to the secondary char formation [36]. Cellulose, known for its strong charring properties, typically produces a char yield of 13–27 %. In contrast, PE has a much lower char-forming tendency, with Liu et al. [35] and Li et al. [37] reporting minimal residues of 0.7 wt% and 0.9 wt%, respectively. At higher temperatures within this stage, steam reacted with C_xH_y and residual char, resulting in the formation of DTG peaks between 605 and 640 °C.

In stage IV (800–900 °C), a minimal weight reduction of 2.5–4.7 wt% was observed. Siddiqui et al. [29] reported a slightly higher weight loss of 6.4 and 5.4 wt% for two BCs samples, attributing this to the gradual decomposition of residuals. Once the char gasification was complete and aluminium foil was inactive, so the mass loss in this stage could be attributed to inorganics decomposition, e.g. calcium carbonate [31]. The minor peak at 826 °C further confirmed the thermal decomposition of calcium carbonate filler.

Fig. 1c–e shows the FTIR spectra of products formed during decomposition of BCs samples. The spectral analysis identified prominent peaks at 4000-3500 cm^{-1} (O-H stretching), 2987-2758 cm^{-1} (C-H stretching), 1841-1636 cm^{-1} (C=O stretching), and 1315-992 cm^{-1} (C-O/C-C stretching). In addition, bands at 2380–2269 and 742-618 cm^{-1} corresponded to CO_2 asymmetric stretching and doubly degenerate bending, respectively. Vibrations at 2218-2047 cm^{-1} were linked to gaseous CO stretching, while those at 1484-1339 cm^{-1} were associated with C=C stretching. The evolution of infrared intensity with temperature demonstrated that the highest concentrations of evolved products were released at 250–450 °C, consistent with DTG peak temperatures. The evolved gases in stage I were more complex than those in later stages. A comparative analysis of IR spectra at the four DTG peak temperatures revealed prominent bands for C-H, C=O, C=C, and C-O/C-C bond vibrations at 340 °C. At 438 °C, the diversity of evolved products decreased, with a significant C-H bond peak. At higher temperatures of 605 and 626 °C, the intensity of C-H band decreased while CO_2 absorption increased.

The gaseous products released during the BCs degradation (Fig. 1f–i) included propyne/allene (p-C_3H_4/a-C_3H_4), propargyl (C_3H_3), ethylene/carbon monoxide (C_2H_4/CO), vinyl anion (C_2H_3), methanol (CH_3OH), and hydroxyl radicals (OH·). In addition, methane

(CH_4), propene (C_3H_6), butadiene/butyne (C_4H_6), butene (C_4H_8), acetylene (C_2H_2), hydrogen (H_2) and carbon dioxide (CO_2) were observed. The evolution of these products with temperature revealed significant peaks for methane (CH_4), propane (C_3H_6), butane (C_4H_6), ethylene (C_2H_2), acetylene (C_2H_2) and hydroxyl (OH·) and methane (CH_3·) radicals, as well as carbon dioxide (CO_2) and hydrogen (H_2) during stage I. A significant increase in propylene (C_3H_4) and propyne (C_3H_3·) emissions occurred around 345 °C. At 500 °C, substantial yields of C_3H_4 and C_3H_3· were observed, with peaks at around 416 °C and 483 °C, respectively. A distinct peak for ethylene/CO, vinyl anion, and methanol was observed at 483 °C, while C_4H_6, C_4H_8, and H_2 peaked at approximately 408 °C. These results are consistent with previous studies by Fu et al. [28] and del Remedio Hernández et al. [29], who identified a broad distribution of paraffins, olefins, and diolefins during pyrolysis. Furthermore, increased proportions of ethane (C_2H_6), ethene (C_2H_4), and isobutene (C_4H_8) were detected at 400–600 °C. At 800 °C, substantial volatile occurred in two distinct regions of 600–700 °C and 700–800 °C. The peaks observed in the former region for C_3H_4, C_3H_3·, C_2H_4/CO, C_2H_3·, and H_2 were maintained in the latter region, whereas CH_4 and CH_3· showed distinct peak only at 700–800 °C.

3.2. Kinetic modeling

Linear fits were performed on the data within α range of 0.10–0.80 (Fig. 2), showing parallel fit lines between α = 0.10 and 0.55. However, significant discrepancies appeared α = 0.55 and 0.60, implying a possible shift in reaction mechanism [38]. This observation was further supported by the TG analysis, which indicated that the paperboard decomposition was almost completion, while PE devolatilization was still ongoing. R^2 values from the slopes of fit lines showed comparable E_a values across the four model-free methods. All models demonstrated R^2 values exceeding 0.90, except at α = 0.60, where a markedly lower value was observed, indicating a shift in the reaction mechanism. Cai & Chen method consistently produced higher R^2 values, suggesting that it provided a more reliable model for the pyrolysis-gasification of BCs.

E_a values from Cai & Chen model indicated a gradual decrease within α = 0.10–0.60, followed by an increase for α > 0.60. The mean E_a for α = 0.10–0.60 was 60.2 kJ mol^{-1}, predominantly attributable to paperboard decomposition. This value was consistent with 52.01–117.06 kJ mol^{-1} reported by Gao et al. [39] for cellulose pyrolysis in nitrogen. However, it was lower than the values of 105–135 kJ mol^{-1} in CO_2-N_2 atmosphere reported by Chen et al. [40] and 178.38–223.31 kJ mol^{-1} in nitrogen revealed by Yeo et al. [41]. The reduced E_a was attributed to the introduction of steam, which enhanced conversion by introducing additional reaction pathways.

This trend was consistent with the findings of Gomez and Mahinpey [42], who reported lower E_a values for coal steam gasification in comparison to CO_2 gasification. In addition, Shan et al. [43] observed a reduction in E_a with the introduction of steam during propane dehydrogenation. This phenomenon had also been observed during PE devolatilization. For α > 0.60, the average E_a increased significantly and reached 205.9 kJ mol^{-1}. This value was comparable to reported values of 218 kJ mol^{-1} and 242.5 kJ mol^{-1} for the pyrolysis of LDPE and HDPE in nitrogen [44], as well as 249.87 kJ mol^{-1} for LDPE conversion in argon [45]. This elevated E_a suggested a transition in reaction mechanism towards PE devolatilization. This trend in Ea values was consistent with previous reports. Xie et al.

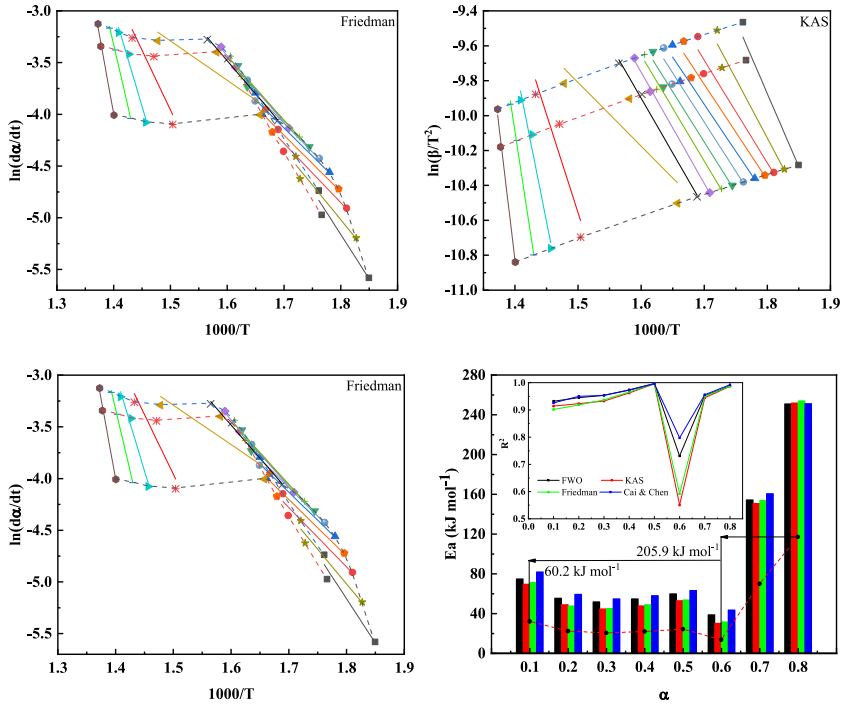

Fig. 2. Resulted Ea and R^2 from four isoconversional methods.

[46] conducted the co-pyrolysis of biomass and polyethylene and found Ea significantly increased from 114.9 to 168.0 kJ mol^{-1} with α increasing from 0.6 to 0.7. Dong et al. [47] also found an increase of Ea with α greater than 0.55.

A comparative analysis of experimental curve with theoretical ones is presented in Fig. 3. For $\alpha < 0.55$, the experimental curve matched with curves from D1, P2, P3, and P4 models. However, a discrepancy was observed between experimental data and these models within α of 0.60–0.90. Among these models, D1 exhibited the highest R^2 values (Table 1), and the calculated E_a was in agreement with that from Cai & Chen method. It indicated that D1 model provided a dependable representation of BCs decomposition.

3.3. Thermodynamic analysis

Three thermodynamics parameters calculated from E_a values from Cai & Chen method are illustrated in Fig. S3. The ΔH followed a similar trend to E_a values, with a mean of 55.3 kJ mol^{-1} for $\alpha < 0.60$ and 201.0 kJ mol^{-1} for $\alpha > 0.60$. The positive ΔH values confirmed the endothermic nature of pyrolysis-gasification, indicating that energy input was required to break down the paperboard and PE structures. The markedly higher ΔH in the later stages ($\alpha > 0.60$) suggested increased heat absorption, mainly for the decomposition of PE matrix and char gasification. The ΔS values were negative for $\alpha \leq 0.60$, indicating a reduction in disorder in products compared to reactants. This suggested that the activated state after thermal decomposition was more ordered than the initial pre-pyrolysis state. However, for $\alpha > 0.60$, ΔS became positive, indicating an increase in disorder and reactivity. This shift indicated that the system initially approached thermodynamic equilibrium before deviating as the reaction progressed, leading to accelerated formation of activated complex. ΔG represented the total energy change associated with the formation of activated complex. The average ΔG was 91.2 kJ mol^{-1} for $\alpha \leq 0.60$ and 121.5 kJ mol^{-1} for $\alpha > 0.60$. Positive ΔG values confirmed the non-spontaneous and endothermic nature of BCs decomposition. Furthermore, the increase in ΔG with temperature indicated a higher energy requirement for BCs decomposition at elevated temperatures. Zhang et al. investigated the pyrolysis of transformer insulating paperboard and found that ΔG increased with conversion rate, implying that the heat absorbed increased during pyrolysis. Bhardwaj et al. [48] also investigated the thermodynamic of paper wastes pyrolysis and found that energy was required for the reagent to reach their transition state.

3.4. ReaxFF-MD simulation

Fig. 4 illustrates the product evolution during steam gasification of a PE/cellulose system at 3000 K. The simulation results demonstrated the formation of various products, including olefins (e.g., C_2H_4, C_3H_6), alkanes (e.g., C_2H_2) and diolefins (e.g., C_3H_4, C_4H_6), as well as H_2, CO, and CO_2. These findings aligned with MS results presented in Fig. 1. The decomposition process can be divided into distinct phases. In the initial phase (<50 ps), a notable release of acetic acid ($C_2H_4O_2$) from cellulose chains was observed. In the primary stage (t > 50 ps), the degradation of PE commenced as the heat energy exceeded the bond dissociation energies of PE backbone and hydrogen bonds. This resulted in the dissociation of bonds and a rapid increase in the formation of C_2H_4, C_3H_6, and C_4H_6. These olefins were primarily produced via β-scission reactions, thermally activated at temperatures above 2000 K. The initial formed olefins (C_2H_4, C_3H_6, C_4H_6) underwent further decomposition to C_2H_2, C_3H_4, and H_2 via H abstraction, facilitated by the high-density reaction environment within the simulation domain. In addition, larger molecules can degraded by radical addition mechanisms in which reactive radicals attacked and fragmented molecular structures.

Fig. 5 illustrates the distribution of products at different temperatures. As temperature increased, the decomposition process favored the formation of smaller gaseous species, particularly C0 and C1 fragments. At 1800 K, product formation was minimal due to

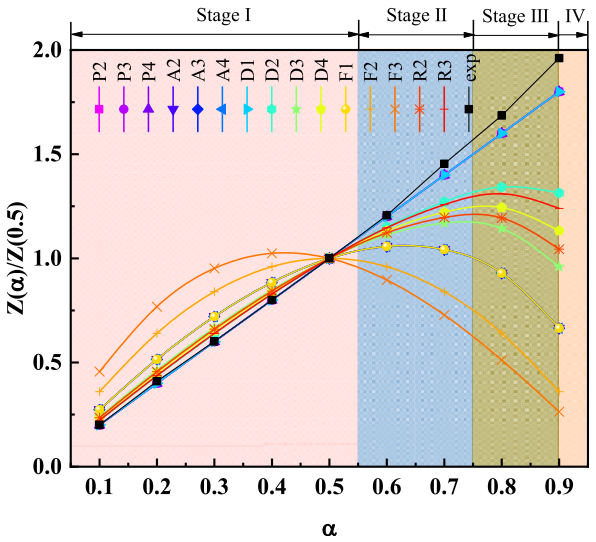

Fig. 3. Probing of reaction mechanism function.

Table 1
Ea, A and R^2 values from CR method.

Mechanism functions	10 K/min			20 K/min			30 K/min		
	Ea (kJ mol^{-1})	A (min^{-1})	R^2	Ea (kJ mol^{-1})	A (min^{-1})	R^2	Ea (kJ mol^{-1})	A (min^{-1})	R^2
P2	28.23	4.50E-02	0.809	31.73	6.48E-02	0.985	16.53	1.48E-03	0.645
P3	15.66	2.14E-03	0.739	17.84	2.78E-03	0.978	7.59	1.43E-04	0.422
P4	9.37	3.74E-04	0.631	10.90	4.70E-04	0.965	3.11	2.71E-05	0.066
A2	36.48	3.72E-01	0.884	40.10	4.86E-01	0.994	22.40	7.08E-03	0.762
A3	21.16	9.94E-03	0.850	23.42	1.20E-02	0.992	11.50	5.04E-04	0.638
A4	13.50	1.36E-03	0.799	15.08	1.59E-03	0.989	6.05	9.88E-05	0.424
F1	82.46	8.59E+03	0.909	90.14	1.45E+04	0.995	55.11	6.51E+00	0.836
F2	101.96	8.40E+05	0.946	109.75	1.13E+06	0.992	69.01	1.60E+02	0.881
F3	124.35	1.53E+08	0.970	132.12	1.56E+08	0.982	84.99	5.93E+03	0.912
D1	141.41	9.20E+08	0.873	156.73	3.60E+09	0.990	97.04	1.03E+04	0.813
D2	151.45	4.74E+09	0.889	166.98	1.70E+10	0.993	104.18	2.58E+04	0.830
D3	162.74	1.43E+10	0.905	178.42	4.61E+10	0.995	112.21	3.47E+04	0.847
D4	155.20	2.51E+09	0.895	170.78	8.70E+09	0.994	106.85	1.04E+04	0.836
R2	73.84	5.54E+02	0.884	81.41	1.03E+03	0.993	48.97	7.75E-01	0.806
R3	76.63	7.18E+02	0.893	84.24	1.29E+03	0.994	50.95	8.24E-01	0.816

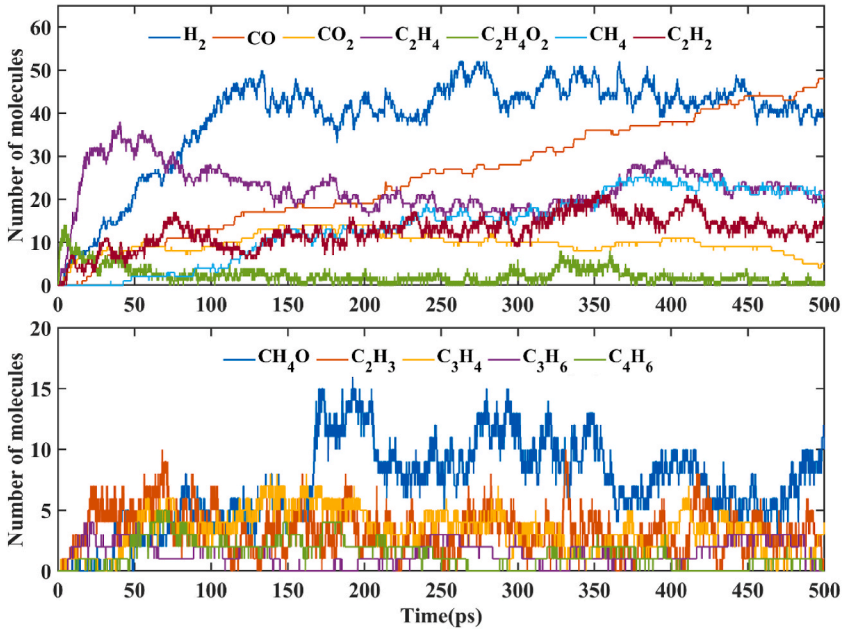

Fig. 4. Products evolution of PE/cellulose system at 3000 K.

insufficient energy for effective pyrolysis and gasification. Most polymer chains remained largely intact, with only minor fragments (C0-C3) being released. The principal products at this stage were H_2O, CO_2, and $C_2H_4O_2$, predominantly resulting from cellulose decomposition, as it has a lower activation energy than PE. At temperatures exceeding 2500 K, the increased thermal energy accelerated the decomposition of both cellulose and PE. A significant increase in evolved products was observed, with a shift in product distribution towards C1 and C2 species, particularly C_2H_4 (PE monomer), due to rapid β-scission reactions. The formation of gaseous species (CO, H_2) also increased, signalling the onset of gasification reactions. At hyperthermal environment, the decomposition process further intensified, leading to the formation of homogeneous gases like CO, CO_2, and H_2. This indicated almost complete decomposition of both PE and cellulose, demonstrating that higher temperatures promoted more extensive molecular fragmentation and gasification.

3.5. Decomposition mechanism and pathway

The paperboard degradation occurred at temperatures below 375 °C, while PE devolatilization occurred between 375 and 500 °C. Charring and steam cracking occurred from 500 to 800 °C, followed by inorganic decomposition between 800 and 900 °C. The thermal decomposition pathway is illustrated in Fig. 6. Cellulose has a relatively high thermal stability, with the maximum degradation rate occurring at around 350 °C. As the temperature increased, cleavage of 1,4-glycosidic bond occurred via an acetal reaction between the

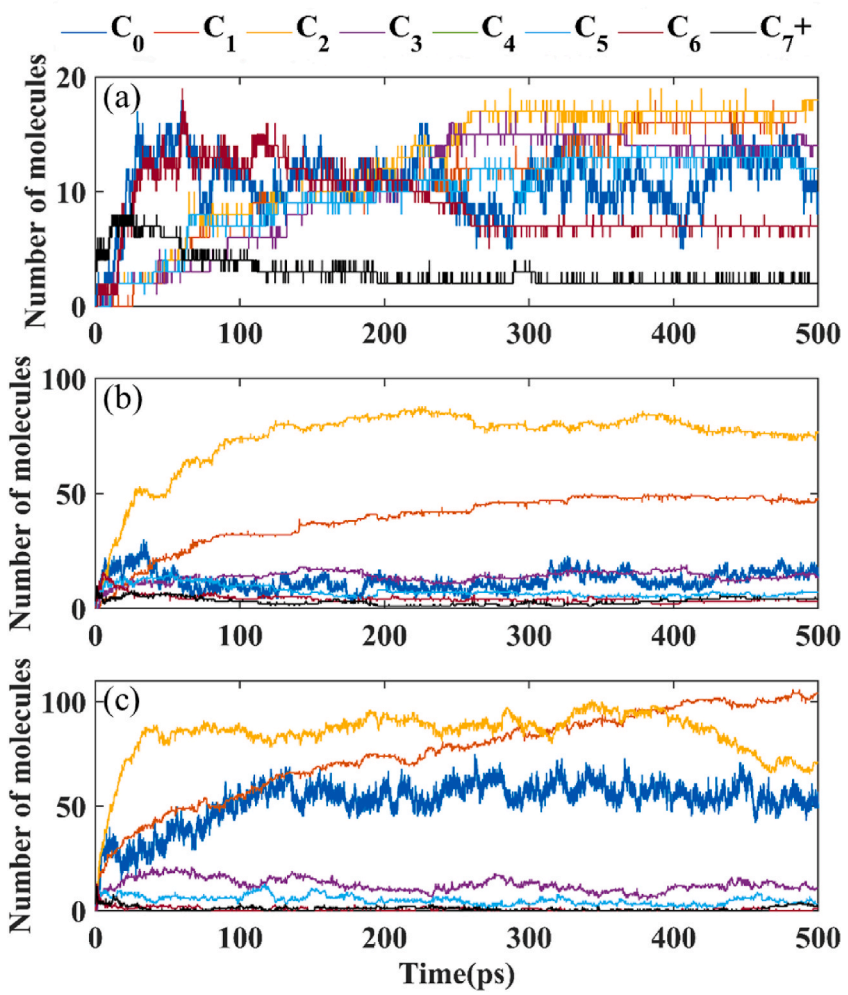

Fig. 5. Products distribution at temperatures of a) 1800 K; b) 2500 K; c) 3000 K.

C1 and C6 carbon atoms, resulting in the release of OH· radicals from C6 position. These radicals then combined with the broken glucosidic bond at C4 position to form levoglucosan (LG). Further isomerization and dehydration of LG gave furan and its derivatives [49,50]. During furan degradation, protonation at the α-carbon induced cleavage of CH_2-O bond, followed by deprotonation. The resulting cumulative diene structure in buta-2,3-dienal (CH_2=C=CH-CHO) was highly unstable and readily converted to propen-1, 3-diene (p-C_3H_4), which could be further isomerized to allene (a-C_3H_4, H_2C=C=CH_2) [51–53]. The formation of p-C_3H_4 could also be attributed to the $CH_3CCHCHCO$ radical from the decomposition of the 2-methylfuran-5-yl radical, which was a key H-abstraction product at C5 position in 2-methylfuran (2-MF) [54]. The formation pathway of C_3H_3· in relation to C_3H_4 is of particular interest. Urness et al. [55] studied the furan pyrolysis and proposed that furan decomposition was a major source of C_3H_3. In contrast, Cheng et al. [56] demonstrated that C_3H_3· was predominantly from C_3H_4, rather than from furan. In this study, 1,2-butadienal was not observed, but butyne was detected, suggesting that the formation of C_3H_4 was predominantly controlled by 2-MF degradation. The evolution of C_3H_3· followed a similar trend to that of C_3H_4, further supporting that C_3H_3· was predominantly derived from C_3H_4 via H-abstraction reactions. In addition, furan can serve as an intermediate in the formation of tetrahydrofuran by hydrogenation, which may subsequently undergo dehydration to produce 1-C_4H_8, C_4H_6, and C_3H_6 [57]. In addition, C_2H_2 and CH_3· can be generated via the reaction: p-C_3H_4 + H· ↔ C_2H_2 + CH_3·.

During PE pyrolysis, homolytic cleavage of C-C bond occurred, either by random or end-chain scission, resulting in the formation of two radicals. Subsequently, hydrogen transfer reactions occurred to form stable secondary or tertiary radicals. Further decomposition involved C-C bond cleavage via β-scission, producing a number of olefins and additional radicals. In the termination phase, disproportionation reactions involving hydrogen abstraction led to the formation of alkanes. In particular, hydrogen migration between radicals played a crucial role in alkanes formation, whereas β-scission of radicals was the dominant pathway for olefin formation. In this study, olefins were identified as the predominant products, confirming that β-scission was the primary reaction mechanism. With respect to CH_3OH formation, two main pathways were identified as shown in eqs. (14) and (15). A comparison CO_2 and CO evolution rates revealed that the trend for CO_2 closely mirrored that of CH_3OH, indicating that CO_2 hydrogenation was a predominant

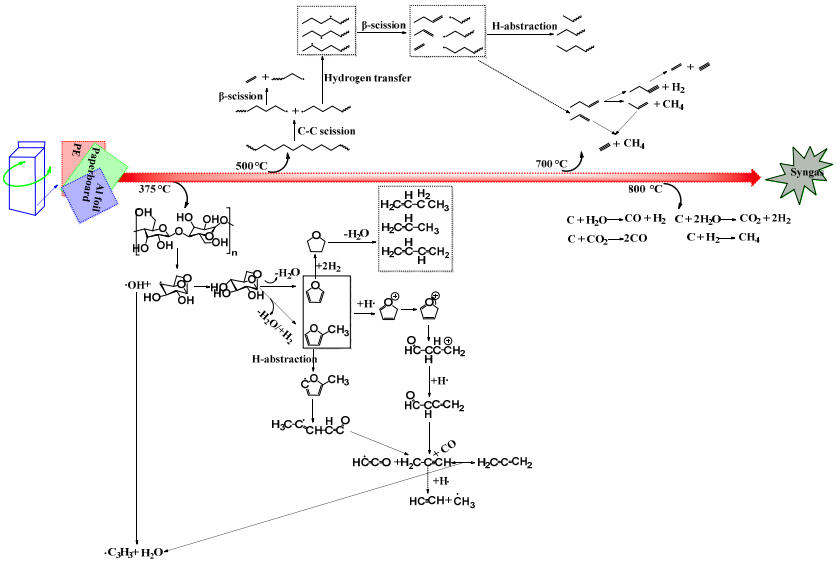

Fig. 6. Thermal decomposition mechanism of BCs.

mechanism contributing to CH_3OH formation.

$$CO_2 + 3H_2 \leftrightarrow CH_3OH + H_2O \quad (14)$$

$$CO + 2H_2 \leftrightarrow CH_3OH \quad (15)$$

When the temperature reached 700 °C, olefins such as C_3H_6 and C_4H_8 underwent hydrogenation and steam cracking, leading to a decrease in their concentration and a corresponding increase in the formation of smaller molecules, including C_3H_4, C_2H_2, and C_2H_4. Further increasing temperature to 800 °C resulted in increased production of methane (CH_4) and hydrogen (H_2), mainly due to reduction reactions.

3.6. TEA results

3.6.1. Capital cost estimation

A factorial methodology was used to systematically estimate the capital investment requirements for different plant scales. Fig. S4 depicts the TPEC, FCI, and TCI calculated for each scale. For the small-scale plant, TPEC was established at €220,000 based on the selected equipment. After applying the installation factors defined in the methodology, FCI was observed to increase by 30 % to €287,760. The inclusion of additional indirect costs resulted in a TCI of €330,924. For the medium plant, the benefits of economies of scale became apparent. The doubling of capacity resulted in an almost tenfold increase in TPEC to €2.2 million. FCI for this scale increased proportionally to €2.88 million, representing a 30 % premium over TPEC. The sub-linear increase in installation costs resulted in a TCI of approximately €3.3 million. For the large plant, TPEC increased further to €2.8 million. Despite having four times the capacity of medium plant, FCI reached €3.7 million, indicating a moderate 30 % premium over TPEC. This suggests that the proportion of installation costs relative to the TPEC decreases as scale increases. As a result, the TCI for this large plant was €4.2 million.

3.6.2. Economic performance across scales

Table 2 shows the principal economic indicators estimated for the three plant scales. SCC was employed as a measure to compare

Table 2
Estimated economic performance of different gasification plants.

Scale (tonne/a)	15000	30000	45000
SCC (€ kWh^{-1})	0.014	0.055	0.039
ASR (€)	1,693,941.48	4,234,853.76	7,622,736.78
GP (€)	18,049.08	618,329.76	2,273,160.78
PBP (years)	15.94	4.65	1.61
ROI (%)	5.5	18.7	54.0
NPV (€)	77,447.96	2,653,230.85	9,754,051.39

the capital intensity of evaluated scales. For the small-scale plant, SCC was calculated at €0.014/kWh, indicating a high capital requirement per unit of electricity generated. This high cost highlighted the challenges faced by smaller plants, which often fail to benefit from economies of scale. For the medium-scale plant, efficiencies began to emerge, reflecting in an SCC of €0.055/kWh. In contrast, the large-scale plant showed a further reduction in SCC to €0.039/kWh. Despite handling a higher throughput, the large plant demonstrated superior capital efficiency compared to its medium counterpart. This reduction in SCC confirmed the existence of economies of scale, allowing a more efficient allocation of capital investment per kWh of electricity produced. As a result, the large-scale plant presented a more attractive investment option, offering higher returns and improved capital efficiency. Similar trends were observed by Do et al. [58] for a woodchip power plant using circulating fluidized bed gasification.

Annual sales revenue (ASR) refers to the total revenue generated by a gasification plant over the course of a year. As illustrated in Table 2, a notable increase in ASR was found along with plant scale, ranging from €1,693,941.48 for the smallest plant to €7,622,736.78 for the largest plant. This trend highlighted the revenue generating potential of larger gasification projects, which benefit from higher production volumes and increased electricity sales. GP represents the difference between annual sales revenue and total production costs, offering insights into plant profitability. Similarly to ASR, GP values increased significantly with plant scales, from €18,049.08 for the smallest plant to €2,273,160.78 for the largest. This trend served to illustrate the economies of scale and revenue benefits associated with larger plants, contributing to improved profitability and financial performance. PBP represents the time required to recuperate its initial capital investment through cash inflows. The data demonstrated a notable reduction with increasing in plant scale, declining from 15.94 years for the smallest plant to 4.65 years for the medium-scale plant and further to 1.61 years for the large plant. This pattern highlighted the shorter capital recovery periods and improved investment returns associated with large-scale gasification projects, reinforcing their economic viability and investment attractiveness. Similarly, Gao et al. [59] reported a PBP of 5.7 years for a medium-sized integrated gasification power generation cycle using wood biomass, further supporting these findings. In conclusion, the trends in ASR, GP, and PBP demonstrated that while revenues increased in line with throughput, the reduction in capital intensity reached a tipping point beyond a certain scale. Among the options evaluated, the large plant emerges as the optimal choice, achieving an effective balance between capital efficiency and revenue potential within the prevailing cost structures.

ROI measures the average annual gross profit as a percentage of the TCI. ROI values varied significantly between different plant scales, with the highest ROI observed in the large plant. The average annual return on TCI for this plant was approximately 54.0 %, while the small-scale and medium-scale plants had comparatively lower ROI values of 5.5 % and 18.7 %, respectively. These variations highlighted different levels of profitability and return on investment associated with different plant scales. Higher NPV values indicate greater profitability and more favorable project returns. In line with the ROI trend, the large plant had the highest NPV at €9,754,051.39, followed by the medium plant at €2,653,230.85. In contrast, the small-scale plant exhibited a markedly lower NPV of €77,447.96, underlining its lower financial viability. These NPV figures illustrated the financial disparity between gasification projects at varying scales, with larger plants demonstrating higher profitability and superior economic performance. The variations in ROI and NPV across plant scales underscored the critical role of scales in assessing the financial viability of gasification projects. Larger-scale plants generally offer higher revenue potential, enhanced profitability, and superior investment returns, making them more attractive to investors than smaller counterparts.

3.6.3. Carbon emissions reduction potential

Previous lifecycle assessment studies have yielded valuable insights into the carbon emissions associated with different energy generation technologies. For example, Ramachandran et al. [60] reported annual net emission savings of 138.9 million to 165.9 million kg of CO_2 equivalent from co-gasification of wood and sludge. Similarly, Parascanu et al. [61] demonstrated that the gasification of sugarcane bagasse resulted in relatively low carbon dioxide emissions of 0.49 kg CO_2eq per megajoule of electricity produced. A significant reduction compared to conventional coal-fired power plants, which typically releases approximately 1.25 kg of CO_2 per kWh of electricity. Further research by Tang et al. [62] and Ouedraogo et al. [63] indicated that the potential of integrating biomass gasification with combined cycle technology to achieve significant carbon emissions. Zang et al. [64] reported emission reductions ranging from 875 to 1,077 kg CO_2eq per MWh, confirming the environmental benefits of biomass gasification for power generation. These results underlined the role of gasification technology in reducing carbon emissions and positioning it as a promising solution for migrating climate change. The relative low carbon footprint of gasification-based electricity generation provides a compelling opportunity for countries such as China to transition towards cleaner energy sources and to reduce their overall carbon emissions. In addition, China's implementation of the National Emissions Trading Scheme provides a economic framework to encourage the adoption of low-carbon technologies. The scheme allocates carbon emission allowances to companies, allowing these emitting below their allocated limits to trade surplus allowances with higher emitters. This market-driven mechanism effectively internalizes the cost of carbon, incentivising investment in cleaner energy solutions and accelerating the transition to a sustainable energy future.

4. Conclusion

The pyrolysis-gasification conversion of BCs was comprehensively studied from both micro- and macroscopic perspectives. TG-DTG analyses revealed mass losses ranging from 90.0 to 95.5 % during the decomposition of BCs. The conversion can be separated into distinct stages of paper decomposition, PE degradation, charring and gasification, and inorganics decomposition. FTIR spectroscopy identified major absorption peaks at 4000–3500, 2987–2758, 1841–1636, and 1315–992 cm^{-1}, which were ascribed to the stretching vibrations of OH, C-H, C=O, and C-O/C-C, respectively. MS analysis identified a number of evolved products, including C_3H_4, C_2H_4, CH_3OH, CH_4, C_3H_6, C_4H_6, C_4H_8, C_2H_2, H_2 and CO_2, highlighting their potential as fuel gases. Ea from four model-free methods showed

a consistent trend, initially decreasing within α of 0.10–0.60, followed by a sharp increase beyond this range. D1 diffusion model demonstrated highest R^2 values and comparable Ea values, confirming its reliability in modeling BC decomposition. Positive values for ΔH and ΔG implied that the pyrolysis-gasification reaction is endothermic and non-spontaneous. ReaxFF-MD simulation were in close agreement with MS results, with β-scission of radicals identified as the principal route for olefin formation. With temperature increasing, the degraded species notably increased, resulting in a higher proportion of homogeneous gases. TEA revealed that gasification-based electricity generation has a low carbon footprint. Larger gasification plants were found to be more profitable, offering higher revenue potential, increased profitability return on investment than smaller counterparts. The results of this study will provide important references for the thermal conversion of packaging waste, municipal solid waste and other organic wastes, promoting the circular economy and sustainable energy development.

CRediT authorship contribution statement

Zhitong Yao: Writing – review & editing, Conceptualization. **Denzel Christopher Makepa:** Writing – original draft, Investigation. **Sourav Poddar:** Writing – original draft, Investigation. **Markus Reinmöller:** Writing – original draft, Investigation. **Michael Bertelsen:** Writing – review & editing, Conceptualization. **Jingjing Jiang:** Writing – original draft, Investigation. **Jiayao Tong:** Writing – original draft, Investigation. **Jiuzhuo Cui:** Writing – original draft, Investigation. **Jie Liu:** Writing – original draft, Investigation. **Ivan Miguel De Cachinho Cordeiro:** Writing – review & editing, Conceptualization.

Declaration of competing interest

The authors declare that they have no known competing financial interests or personal relationships that could have appeared to influence the work reported in this paper.

Acknowledgements

This work was financially supported by the Joint Fund of Zhejiang Provincial Natural Science Foundation of China (Grant no. LBMHZ25E060003).

Appendix A. Supplementary data

Supplementary data to this article can be found online at https://doi.org/10.1016/j.csite.2025.106228.

Data availability

No data was used for the research described in the article.

References

[1] S. Xu, Y. Zhai, J. Feng, G. Liu, A framework of carbon-neutral waste transportation: modeling and sensitive analysis, Circ. Econ. 2 (2023), https://doi.org/10.1016/j.cec.2023.100024.
[2] X. Lu, L. Cao, H. Wang, W. Peng, J. Xing, S. Wang, S. Cai, B. Shen, Q. Yang, C.P. Nielsen, M.B. McElroy, Gasification of coal and biomass as a net carbon-negative power source for environment-friendly electricity generation in China, Proc. Natl. Acad. Sci. U. S. A. 116 (2019), https://doi.org/10.1073/pnas.1812239116.
[3] P. Gururani, P. Bhatnagar, B. Bisht, K.K. Jaiswal, V. Kumar, S. Kumar, M.S. Vlaskin, A.V. Grigorenko, K.G. Rindin, Recent advances and viability in sustainable thermochemical conversion of sludge to bio-fuel production, Fuel 316 (2022), https://doi.org/10.1016/j.fuel.2022.123351.
[4] A. Tencati, S. Pogutz, B. Moda, M. Brambilla, C. Cacia, Prevention policies addressing packaging and packaging waste: some emerging trends, Waste Manag. 56 (2016), https://doi.org/10.1016/j.wasman.2016.06.025.
[5] B. Kou, Q. Shi, S. Wang, R. Ji, H. Zhao, Y. Mi, C. Li, Co-evolution with pore and molecular structure during tar-rich coal pyrolysis, Case Stud. Therm. Eng. 62 (2024) 105215.
[6] Z. Huang, T. Zhang, C. Wang, W. Xiao, Z. Wang, O. Tursunov, J. Wu, Y. Zhou, X. Yao, G. Li, Exploring the factors influencing the co-pyrolysis of walnut shells, pistachio shells, and polypropylene based on thermal behavior, kinetics and reaction mechanism, Case Stud. Therm. Eng. 65 (2025) 105679.
[7] M.Z. Siddiqui, Y.K. Park, Y. Kang, A. Watanabe, S. Kim, Y.M. Kim, Effective use of aluminum-plastic laminate as a feedstock for catalytic pyrolysis over micro and mesoporous catalysts, J. Clean. Prod. 229 (2019), https://doi.org/10.1016/j.jclepro.2019.04.404.
[8] Y. Wang, Y. Wang, Y. Zhu, C. Fang, D. Xu, X. Zheng, Interactions of the main components in paper-plastic-aluminum complex packaging wastes during the hydrothermal liquefaction process, Chem. Eng. Technol. 44 (2021), https://doi.org/10.1002/ceat.202100124.
[9] J. Haydary, D. Susa, J. DudáŠ, Pyrolysis of aseptic packages (tetrapak) in a laboratory screw type reactor and secondary thermal/catalytic tar decomposition, Waste Manag. 33 (2013), https://doi.org/10.1016/j.wasman.2013.01.031.
[10] A.C.T. Van Duin, S. Dasgupta, F. Lorant, W.A. Goddard, ReaxFF: a reactive force field for hydrocarbons, J. Phys. Chem. A 105 (2001), https://doi.org/10.1021/jp004368u.
[11] Z.G. Yan, J.F. Zeng, Y. Xiao, Z.P. Wang, Q.W. Li, X. Lu, Exploring carbon dioxide generation in combustion of long-flame coal in Huating mining area by using ReaxFF MD, Case Stud. Therm. Eng. 55 (2024), https://doi.org/10.1016/j.csite.2024.104171.
[12] W. Xuan, H. Wang, S. Yan, D. Xia, Exploration on the steam gasification mechanism of waste PE plastics based on ReaxFF-MD and DFT methods, Fuel 315 (2022), https://doi.org/10.1016/j.fuel.2021.123121.
[13] D. Hong, L. Liu, C. Wang, T. Si, X. Guo, Construction of a coal char model and its combustion and gasification characteristics: molecular dynamic simulations based on ReaxFF, Fuel 300 (2021), https://doi.org/10.1016/j.fuel.2021.120972.

[14] Y. Pang, X. Zhu, N. Li, Z. Wang, Investigation on reaction mechanism for CO_2 gasification of softwood lignin by ReaxFF MD method, Energy 267 (2023), https://doi.org/10.1016/j.energy.2022.126533.
[15] I.M. De Cachinho Cordeiro, T.B.Y. Chen, A.C.Y. Yuen, Q. Chen, W. Yang, C. Wang, W. Wang, Q.N. Chan, J. Zhang, G.H. Yeoh, Characterising flame-retardant mechanism of phosphorous-containing intumescent coating on polyethylene via ReaxFF MD simulations, Chem. Eng. J. 480 (2024), https://doi.org/10.1016/j.cej.2023.148169.
[16] S. Yousef, J. Eimontas, N. Striūgas, M.A. Abdelnaby, Effect of aluminum leaching pretreatment on catalytic pyrolysis of metallised food packaging plastics and its linear and nonlinear kinetic behaviour, Sci. Total Environ. 844 (2022), https://doi.org/10.1016/j.scitotenv.2022.157150.
[17] Z. Yao, S. Yu, W. Su, W. Wu, J. Tang, W. Qi, Kinetic studies on the pyrolysis of plastic waste using a combination of model-fitting and model-free methods, Waste Manag. Res. 38 (2020), https://doi.org/10.1177/0734242X19897814.
[18] J.L.F. Alves, J.C.G. da Silva, G.D. Mumbach, S. Arias, J.G.A. Pacheco, M. Di Domenico, C. Marangoni, Valorization of royal palm tree agroindustrial waste via pyrolysis with a focus on physicochemical properties, kinetic triplet, thermodynamic parameters, and volatile products, Biomass Bioenergy 177 (2023), https://doi.org/10.1016/j.biombioe.2023.106937.
[19] I. Mohan, A.K. Panda, S. Mandal, S. Kumar, Co-pyrolysis of Azadirachta indica non-edible seed and waste LDPE: analysis of kinetic models using thermogravimetric analyser and prediction modeling with Artificial Neural Network (ANN), Fuel 350 (2023), https://doi.org/10.1016/j.fuel.2023.128765.
[20] Z. Yao, P. Romano, W. Fan, S. Gautam, N. Tippayawong, C. Jaroenkhasemmeesuk, J. Liu, X. Wang, W. Qi, Probing pyrolysis conversion of separator from spent lithium-ion batteries: thermal behavior, kinetics, evolved gas analysis and aspen plus modeling, Case Stud. Therm. Eng. 63 (2024) 105342, https://doi.org/10.1016/j.csite.2024.105342.
[21] Z. Yao, J. Tong, R.F.B. Gonçalves, A. Kumar, N. Manić, F. Vegliò, P. Romano, J. Jiang, J. Cui, J. Liu, Recycling of end-of-life solar panels: focusing on the pyrolysis conversion of back sheet from a micro perspective, J. Clean. Prod. (2025) 144796.
[22] K. Chenoweth, A.C.T. Van Duin, W.A. Goddard, ReaxFF reactive force field for molecular dynamics simulations of hydrocarbon oxidation, J. Phys. Chem. A 112 (2008), https://doi.org/10.1021/jp709896w.
[23] M.M. Samy, M.M. Elazazy, Optimal sizing and techno-economic analysis of reverse osmosis desalination systems based on PV/Wind green energy system, J. Eng. Sci. Sustain. Ind. Technol. 2 (2024) 33–39.
[24] A.F. Güven, S. Barakat, M.M. Samy, Optimal design and cost analysis of a hybrid renewable energy system for a small hotel based on the Arctic Puffin optimization algorithm, in: 2024 25th International Middle East Power System Conference (MEPCON), IEEE, 2024, pp. 1–7.
[25] M.M. Samy, M. Nabile, Design and analysis of an islanded green energy station for highways emergency hospitals at different locations in Egypt, J. Eng. Sci. Sustain. Ind. Technol. 2 (2024) 17–27.
[26] E.M. Sayed, K.H. Ibrahiem, A. Farhan, M.M. Samy, Feasibility analysis and techno-economic study for green energy system connected to unhealthy grid, in: 2024 25th International Middle East Power System Conference (MEPCON), IEEE, 2024, pp. 1–6.
[27] G. Towler, R. Sinnott, Chemical engineering design: principles, practice and economics of plant and process design. https://doi.org/10.1016/B978-0-12-821179-3.01001-3, 2021.
[28] M.S. Peters, J.I. Peters, Plant design and economics for chemical engineers, Eng. Econ. 5 (1959), https://doi.org/10.1080/00137915908965075.
[29] M.Z. Siddiqui, T.U. Han, Y.K. Park, Y.M. Kim, S. Kim, Catalytic pyrolysis of tetra pak over acidic catalysts, Catalysts 10 (2020), https://doi.org/10.3390/catal10060602.
[30] A.K. Figen, E. Terzi, N. Yilgör, S.N. Kartal, S. Pişkin, Thermal degradation characteristic of Tetra Pak panel boards under inert atmosphere, Kor. J. Chem. Eng. 30 (2013), https://doi.org/10.1007/s11814-012-0185-y.
[31] H. Huo, Y. Ma, TG/DTA-FTIR study on total resource recovery from Tetra Pak waste by pyrolysis under a CO_2 environment, Prog. React. Kinet. Mech. 43 (2018), https://doi.org/10.3184/146867818X15233705894437.
[32] J. Xu, S. Su, Z. Sun, M. Qing, Z. Xiong, Y. Wang, L. Jiang, S. Hu, J. Xiang, Effects of steam and CO_2 on the characteristics of chars during devolatilization in oxy-steam combustion process, Appl. Energy 182 (2016), https://doi.org/10.1016/j.apenergy.2016.08.121.
[33] P. Mellin, X. Yu, W. Yang, W. Blasiak, Influence of reaction atmosphere (H_2O, N_2, H_2, CO_2, CO) on fluidized-bed fast pyrolysis of biomass using detailed tar vapor chemistry in computational fluid dynamics, Ind. Eng. Chem. Res. 54 (2015), https://doi.org/10.1021/acs.iecr.5b02164.
[34] L.M. Alvarenga, T.P. Xavier, M.A.S. Barrozo, M.S. Bacelos, T.S. Lira, Determination of activation energy of pyrolysis of carton packaging wastes and its pure components using thermogravimetry, Waste Manag. 53 (2016), https://doi.org/10.1016/j.wasman.2016.04.015.
[35] X. Liu, K. Tian, Z. Chen, W. Wei, B. Xu, B.J. Ni, Online TG-FTIR-MS analysis of the catalytic pyrolysis of polyethylene and polyvinyl chloride microplastics, J. Hazard Mater. 441 (2023), https://doi.org/10.1016/j.jhazmat.2022.129881.
[36] D. Shen, R. Xiao, S. Gu, K. Luo, The pyrolytic behavior of cellulose in lignocellulosic biomass: a review, RSC Adv. 1 (2011), https://doi.org/10.1039/c1ra00534k.
[37] D. Li, S. Lei, G. Rajput, L. Zhong, W. Ma, G. Chen, Study on the co-pyrolysis of waste tires and plastics, Energy 226 (2021), https://doi.org/10.1016/j.energy.2021.120381.
[38] B. Wang, Z. Yao, M. Reinmöller, N. Kishore, F. Tesfaye, R. Luque, Pyrolysis behavior, kinetics, and thermodynamics of waste pharmaceutical blisters under CO_2 atmosphere, J. Anal. Appl. Pyrolysis 170 (2023), https://doi.org/10.1016/j.jaap.2023.105883.
[39] Z. Gao, N. Li, M. Chen, W. Yi, Comparative study on the pyrolysis of cellulose and its model compounds, Fuel Process. Technol. 193 (2019), https://doi.org/10.1016/j.fuproc.2019.04.038.
[40] T. Chen, J. Wu, J. Zhang, J. Wu, L. Sun, Gasification kinetic analysis of the three pseudocomponents of biomass-cellulose, semicellulose and lignin, Bioresour. Technol. 153 (2014), https://doi.org/10.1016/j.biortech.2013.12.021.
[41] J.Y. Yeo, B.L.F. Chin, J.K. Tan, Y.S. Loh, Comparative studies on the pyrolysis of cellulose, hemicellulose, and lignin based on combined kinetics, J. Energy Inst. 92 (2019), https://doi.org/10.1016/j.joei.2017.12.003.
[42] A. Gomez, N. Mahinpey, Kinetic study of coal steam and CO_2 gasification: a new method to reduce interparticle diffusion, Fuel 148 (2015), https://doi.org/10.1016/j.fuel.2015.01.071.
[43] Y. Shan, Z. Sui, Y. Zhu, D. Chen, X. Zhou, Effect of steam addition on the structure and activity of Pt-Sn catalysts in propane dehydrogenation, Chem. Eng. J. 278 (2015), https://doi.org/10.1016/j.cej.2014.09.107.
[44] A. Aboulkas, K. El harfi, A. El Bouadili, Thermal degradation behaviors of polyethylene and polypropylene. Part I: pyrolysis kinetics and mechanisms, Energy Convers. Manag. 51 (2010), https://doi.org/10.1016/j.enconman.2009.12.017.
[45] Y. Zheng, L. Tao, X. Yang, Y. Huang, C. Liu, Z. Zheng, Study of the thermal behavior, kinetics, and product characterization of biomass and low-density polyethylene co-pyrolysis by thermogravimetric analysis and pyrolysis-GC/MS, J. Anal. Appl. Pyrolysis 133 (2018), https://doi.org/10.1016/j.jaap.2018.04.001.
[46] T. Xie, L. Zhao, Z. Yao, K. Kang, J. Jia, T. Hu, X. Zhang, Y. Sun, L. Huo, Co-pyrolysis of biomass and polyethylene: insights into characteristics, kinetic and evolution paths of the reaction process, Sci. Total Environ. 897 (2023) 165443, https://doi.org/10.1016/j.scitotenv.2023.165443.
[47] R. Dong, Z. Tang, H. Song, Y. Chen, X. Wang, H. Yang, H. Chen, Co-pyrolysis of vineyards biomass waste and plastic waste: thermal behavior, pyrolytic characteristic, kinetics, and thermodynamics analysis, J. Anal. Appl. Pyrolysis 179 (2024) 106506, https://doi.org/10.1016/j.jaap.2024.106506.
[48] G. Bhardwaj, M. Kumar, P.K. Mishra, S.N. Upadhyay, Kinetic analysis of the slow pyrolysis of paper wastes, Biomass Convers. Biorefin (2021) 1–14.
[49] K. Tomishige, M. Yabushita, J. Cao, Y. Nakagawa, Hydrodeoxygenation of potential platform chemicals derived from biomass to fuels and chemicals, Green Chem. 24 (2022), https://doi.org/10.1039/d2gc01289h.
[50] Q. Zhao, B.M. Savoie, Deep reaction network exploration of glucose pyrolysis, Proc. Natl. Acad. Sci. U. S. A. 120 (2023), https://doi.org/10.1073/PNAS.2305884120.
[51] B. Sun, H. Liang, D. Che, H. Liu, S. Guo, Mechanistic investigation of CO generation by pyrolysis of furan and its main derivatives, RSC Adv. 9 (2019), https://doi.org/10.1039/c8ra10106j.

[52] S. Panigrahy, J. Liang, S.S. Nagaraja, Z. Zuo, G. Kim, S. Dong, G. Kukkadapu, W.J. Pitz, S.S. Vasu, H.J. Curran, A comprehensive experimental and improved kinetic modeling study on the pyrolysis and oxidation of propyne, Proc. Combust. Inst. 38 (2021), https://doi.org/10.1016/j.proci.2020.06.320.
[53] D. Liu, C. Togbé, L.S. Tran, D. Felsmann, P. Oßwald, P. Nau, J. Koppmann, A. Lackner, P.A. Glaude, B. Sirjean, R. Fournet, F. Battin-Leclerc, K. Kohse-Höinghaus, Combustion chemistry and flame structure of furan group biofuels using molecular-beam mass spectrometry and gas chromatography - part I: furan, Combust. Flame 161 (2014), https://doi.org/10.1016/j.combustflame.2013.05.028.
[54] L.S. Tran, C. Togbé, D. Liu, D. Felsmann, P. Oßwald, P.A. Glaude, R. Fournet, B. Sirjean, F. Battin-Leclerc, K. Kohse-Höinghaus, Combustion chemistry and flame structure of furan group biofuels using molecular-beam mass spectrometry and gas chromatography - part II: 2-Methylfuran, Combust. Flame 161 (2014), https://doi.org/10.1016/j.combustflame.2013.05.027.
[55] K.N. Urness, Q. Guan, A. Golan, J.W. Daily, M.R. Nimlos, J.F. Stanton, M. Ahmed, G.B. Ellison, Pyrolysis of furan in a microreactor, J. Chem. Phys. 139 (2013), https://doi.org/10.1063/1.4821600.
[56] Z. Cheng, Y. Tan, L. Wei, L. Xing, J. Yang, L. Zhang, Y. Guan, B. Yan, G. Chen, D.Y.C. Leung, Experimental and kinetic modeling studies of furan pyrolysis: fuel decomposition and aromatic ring formation, Fuel 206 (2017), https://doi.org/10.1016/j.fuel.2017.05.090.
[57] A. Kuznetsov, G. Kumar, M.A. Ardagh, M. Tsapatsis, Q. Zhang, P.J. Dauenhauer, On the economics and process design of renewable butadiene from biomass-derived furfural, ACS Sustain. Chem. Eng. 8 (2020), https://doi.org/10.1021/acssuschemeng.9b06881.
[58] T.X. Do, Y. il Lim, H. Yeo, U. do Lee, Y. tai Choi, J. hun Song, Techno-economic analysis of power plant via circulating fluidized-bed gasification from woodchips, Energy 70 (2014), https://doi.org/10.1016/j.energy.2014.04.048.
[59] Z. Gao, J. Miao, J. Zhao, M. Mesri, Comprehensive economic analysis and multi-objective optimization of an integrated gasification power generation cycle, Process Saf. Environ. Prot. 155 (2021), https://doi.org/10.1016/j.psep.2021.09.007.
[60] S. Ramachandran, Z. Yao, S. You, T. Massier, U. Stimming, C.H. Wang, Life cycle assessment of a sewage sludge and woody biomass co-gasification system, Energy 137 (2017), https://doi.org/10.1016/j.energy.2017.04.139.
[61] M.M. Parascanu, M. Kaltschmitt, A. Rödl, G. Soreanu, L. Sánchez-Silva, Life cycle assessment of electricity generation from combustion and gasification of biomass in Mexico, Sustain. Prod. Consum. 27 (2021), https://doi.org/10.1016/j.spc.2020.10.021.
[62] Y. Tang, J. Dong, G. Li, Y. Zheng, Y. Chi, A. Nzihou, E. Weiss-Hortala, C. Ye, Environmental and exergetic life cycle assessment of incineration- and gasification-based waste to energy systems in China, Energy 205 (2020), https://doi.org/10.1016/j.energy.2020.118002.
[63] A.S. Ouedraogo, R.S. Frazier, A. Kumar, Comparative life cycle assessment of gasification and landfilling for disposal of municipal solid wastes, Energies 14 (2021), https://doi.org/10.3390/en14217032.
[64] G. Zang, J. Zhang, J. Jia, E.S. Lora, A. Ratner, Life cycle assessment of power-generation systems based on biomass integrated gasification combined cycles, Renew. Energy 149 (2020), https://doi.org/10.1016/j.renene.2019.12.013.